Nano Research

Open Access

Research Article

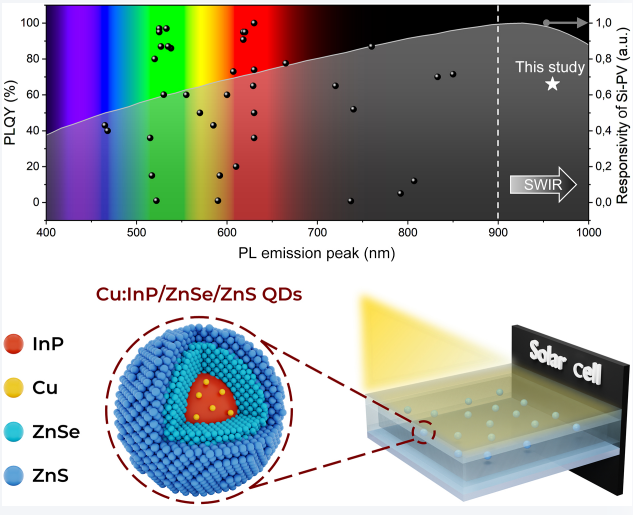
Efficient short-wave infrared emission by copper-doped InP/ZnSe/ZnS quantum dots and their application for luminescent solar concentrators

Tarik Safa Kaya[1], Ugur Berkay Caliskan[2], Parsa Kaviani[2], Asim Onal[3], Eren Tekinay[1], Guncem Ozgun Eren[3], Hande Gunduz[4], Hadi Jahangiri[5], Mehmet Silme[6], Kadriye Kutlay[6], Ugur Unal[7], and Sedat Nizamoglu[2] ✉

[1] *Department of Materials Science and Engineering, Koç University, Istanbul 34450, Türkiye*
[2] *Department of Electrical and Electronics Engineering, Koç University, Istanbul 34450, Türkiye*
[3] *Department of Biomedical Science and Engineering, Koç University, Istanbul 34450, Türkiye*
[4] *Nanofabrication and Nanocharacterization Center for Scientific and Technological Advanced Research, Koç University, Istanbul 34450, Türkiye*
[5] *Koç University Surface Science and Technology Center (KUYTAM), Koç University, Istanbul 34450, Türkiye*
[6] *Berteks Tekstil Sanayi ve Ticaret A.Ş., Bursa 16245, Türkiye*
[7] *Department of Chemistry, Koç University, Istanbul 34450, Türkiye*

Cite this article: *Nano Research*, **2026**, *19*, 94908234. https://doi.org/10.26599/NR.2025.94908234

ABSTRACT: InP quantum dots (QDs) have been a major building block of modern display technology due to their high photoluminescence quantum yield (PLQY) in the visible spectrum, superior stability, and eco-friendly composition. However, their applications at short-wave infrared (SWIR) have been hindered by their low efficiency. Here, we report the synthesis of efficient and SWIR-emitting InP QDs by precisely controlling the InP core nucleation using a low-cost ammonia phosphorus precursor, while avoiding size-limiting $ZnCl_2$ for effective copper doping. Subsequent epitaxial growth of a lattice-matched ZnSe/ZnS multishell enhanced the QD sphericity and surface smoothness and yielded a record PLQY of 66% with an emission peak at 960 nm. When QDs were integrated as the high-refractive-index luminescent core of a liquid waveguide-based luminescent solar concentrator (LSC), the device achieved an optical efficiency of 7.36%. This performance arises from their high PLQY, spectral alignment with the responsivity peak of silicon solar cells, and the optimized core/cladding waveguide structure. These results highlight the potential of InP QDs as a promising nanomaterial for SWIR emission and applications.



KEYWORDS: InP quantum dots, Cu-doping, short-wave infrared, luminescent solar concentrator, optical efficiency

1 Introduction

Colloidal quantum dots (QDs) are a unique class of luminescent nanomaterials with broad-band absorption, tunable emission controlled by quantum confinement effect and compositional variations, high stability, and solution processability [1–7]. Among them, InP-based QDs have emerged as a game-changing nanomaterial for display technology due to their high photoluminescence quantum yield (PLQY) in the visible spectrum and the absence of RoHS-restricted toxic elements such as cadmium (Cd) and lead (Pb) [8–10].

To date, significant advancements have been made in the synthesis of highly efficient and stable InP-based QDs emitting in the visible spectrum. Core InP quantum dots initially exhibited a low PLQY of ~ 1% due to unpassivated surface defects, which introduced trap states [11, 12]. To enhance the luminescence properties, the treatment with hydrofluoric acid (HF) effectively

Received: August 22, 2025; **Revised:** October 22, 2025
Accepted: October 30, 2025

✉Address correspondence to snizamoglu@ku.edu.tr

passivated indium dangling bonds, significantly enhancing the PLQY to 36% [13]. Building on this, the growth of an epitaxial wide-bandgap semiconductor shell (ZnSe or ZnS) on the InP core further enhances the exciton confinement, boosting the PLQY to 60% [14–16]. To reduce the interfacial strain and defect formation, alloy shells such as ZnSeS were developed, offering better lattice matching and enhanced fluorescence stability [17, 18]. In parallel, ion passivation strategies, using Cd^{2+}, Zn^{2+}, or F^-, were shown to efficiently suppress electron and hole traps, with the Cd^{2+} treatment raising PLQY to over 50% even without a shell [19]. Subsequent innovations involved a core/shell/shell architecture featuring an intermediate ZnSe layer to mitigate the lattice mismatch between InP and ZnS, along with an ultrathin ZnS outer shell. This structure achieved an exceptional PLQY of 95% [20]. Moreover, an *in-situ* HF treatment combined with ZnSe/ZnS multishell growth achieved a near-unity PLQY at 630 nm [21].

However, in the short-wave infrared (SWIR) region (0.9–2.0 μm) [22], where applications such as bioimaging probes, biosensors, and luminescent solar concentrators (LSCs) hold significant potential [23], InP QDs exhibit low PLQY, which restricts their usability in this wavelength range (Fig. 1(a)).

A wide variety of strategies have been explored to extend the emission wavelength of InP QDs into the infrared region. For instance, removing $ZnCl_2$ while increasing the phosphorus precursor injection temperature has been shown to shift QD absorption from the red (~ 575 nm) to the near-infrared (NIR) range (~ 720 nm) [24]. Additionally, replacing the indium halide precursor from InI to InCl enables the peak emission wavelength at 730 nm with a PLQY up to 80% [25]. To achieve deeper infrared emission, giant pyramidal InP/ZnS QDs (diameter > 15 nm) were synthesized via high-temperature nucleation followed by low-temperature epitaxial growth. This approach yielded emission at 807 nm [26], though with a PLQY of only 12%.

An alternative approach involves doping InP QDs to introduce midgap states, thereby achieving sub-bandgap emission. Although doping with manganese (Mn) [27, 28], silver (Ag) [29], or ruthenium (Ru) [30] results in red emission, the copper (Cu) doping has been particularly effective in inducing a larger Stokes shift to extend emission from the visible to the near-infrared region. Some InP-based QDs achieved emission wavelengths up to 1.1 μm, but their PLQY remained low (i.e., < 5%) [31]. Although the shell growth improved PLQY, the emission bands generally stayed below the SWIR range [32–35] (Fig. 1(a) and Table S1 in the Electronic Supplementary Material (ESM)).

To harness the potential of InP QDs for LSCs requires emission toward the responsivity peak of silicon solar cells, and recent studies have focused on band-structure and compositional engineering in addition to the conventional doping strategy. Type-II band

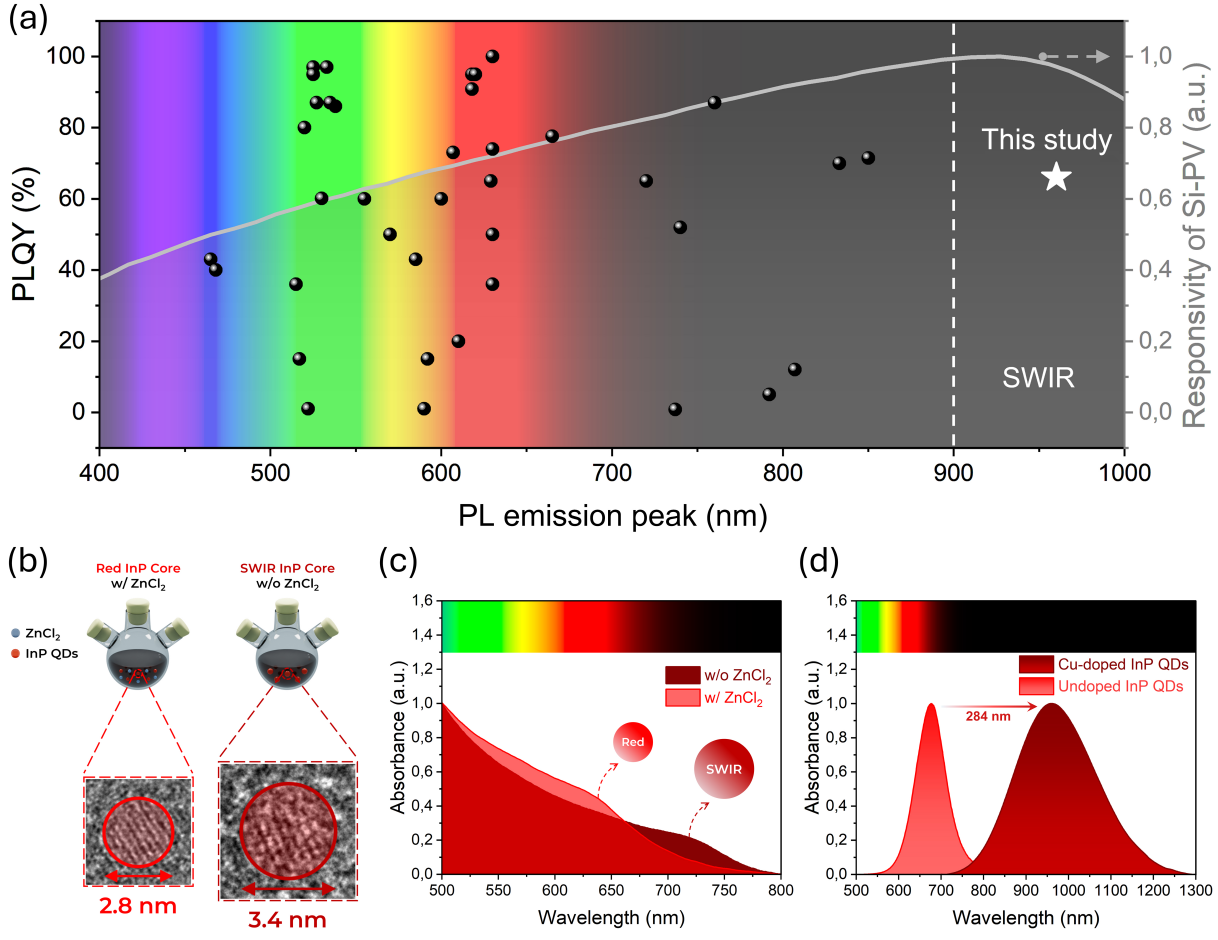


Figure 1 (a) Photoluminescence quantum yields and corresponding emission wavelengths of previous InP QD reports, along with the responsivity of the silicon solar cell (grey line) (Table S1 in the ESM). (b) Transmission electron microscopy images and schematic illustrations of the synthesis process for red- and SWIR-emitting InP QDs, highlighting the critical role of $ZnCl_2$. (c) Absorption spectra of red- and SWIR-emitting InP QDs synthesized with and without $ZnCl_2$, respectively. (d) PL spectra of SWIR-emitting InP QDs before and after the introduction of copper doping.

alignment in InP/ZnO core/shell QDs enables Stokes-shift engineering to suppress reabsorption [36]. Quasi-type-II InP/ZnSe giant pyramidal QDs further reduce reabsorption losses [37]. Beyond shell-based approaches, graded-bandgap InP QD funnels facilitate exciton recycling for enhanced LSC efficiency [38]. Despite these advances, achieving high PLQY in the SWIR range remains a key challenge for InP-based LSCs.

Cu-doped InP QDs are promising luminophores for LSCs owing to their large Stokes shift, which effectively mitigates reabsorption losses, a key bottleneck in achieving high device efficiency [32]. Moreover, their photoluminescence can be precisely tuned across the SWIR region to align with the responsivity peak of silicon solar cells [31]. These combined features make Cu-doping an effective strategy for realizing high-performance, environmentally sustainable LSCs.

In this study, we demonstrate the synthesis of efficient Cu-doped InP/ZnSe/ZnS core/shell/shell QDs emitting in the SWIR region that match with the peak responsivity of silicon solar cells for LSC application (Fig. 1(a)). By using a safe and stable P precursor of tris(diethylamino)phosphine ($(DEA)_3P$) with $InCl_3$, we observed a desired strong red shift in the absorption of InP core after removing the size-limiting $ZnCl_2$ (Figs. 1(b) and 1(c)). After copper doping, the emission peak shifted to 1013 nm with a prolonged lifetime and an improved PLQY from less than 1% to ~ 7%. Subsequent epitaxial growth of lattice-matched ZnSe and ZnS shell growth significantly enhanced the PLQY to 66% with an emission peak at 960 nm (Fig. 1(d)). For the LSC application, QDs were dispersed in high-refractive-index paraffin oil to form the waveguide core, which was surrounded by low-refractive-index polymer cladding layers, and this structure achieved an optical efficiency of 7.36%. These findings highlight the great potential of InP QDs for SWIR applications.

2 Experimental

2.1 Chemicals

Indium(III) chloride ($InCl_3$, 99.999%), tris(diethylamino)phosphine (97%), zinc stearate $Zn(St)_2$, trioctylphosphine (TOP, > 97%), selenium (Se, 99.99%, powder), sulfur (S) (reagent grade, powder, purified by refining, −100 mesh particle size), oleylamine (OAm), octadecene (ODE, %95), copper(II) acetate (powder, 99.99% trace metals basis), and stearic acid (SA, 98%) were purchased from Sigma Aldrich.

2.2 Preparation of copper stearate

1 mmol of $Cu(Ac)_2$ and 2 mmol of SA were stirred in 10 mL of ODE at 150 °C for 1 h. The solution was washed with acetone 5 times via centrifugation at 6000 rpm for 5 min. It was kept in an inert atmosphere.

2.3 Preparation of zinc and sulfur precursors

Zinc stearate ($Zn(St)_2$) (1.5 g) was dispersed in 6 mL of ODE to form Zn-ODE precursor solution. For the selenium and sulfur precursor preparation, 2.2 M stock solution was prepared by dissolving selenium and sulfur in TOP, respectively.

2.4 Synthesis of InP core QDs

For the synthesis of InP core QDs, 100 mg (0.45 mmol) of $InCl_3$ was mixed in 5 mL (15 mmol) of OAm in glovebox. Afterwards, the mixture was stirred continuously while being degassed at 120 °C for one hour and then heated to 200 °C under argon atmosphere. When the mixture temperature reached 200 °C, a volume of 0.45 mL (1.6 mmol) of tris(diethylamino)phosphine was injected and mixed for 30 min at 200 °C. Before copper precursor adding, the aliquot was taken from the main solution for further characterizations.

2.5 Synthesis of copper doped InP core QDs

After the InP QD solution was mixed at 200 °C for 30 min, it was cooled to 120 °C. At this temperature the copper precursor solution was injected and the main solution was heated to 190 °C. The reaction mixture was stirred at 190 °C for 30 min. Before ZnSe and ZnS shelling, the aliquot was taken from the main solution.

2.6 Synthesis of Cu-doped InP/ZnSe/ZnS core/shell/shell QDs

After the Cu:InP synthesis, slow injection of 1.5 mL of saturated TOP-Se (2.2 M) was performed at 200 °C and kept at 200 °C for 60 min. After that, 1 g of $Zn(St)_2$ in 4 mL of ODE was slowly injected into the crude solution and mixed for 30 min. During mixing, the temperature was increased from 200 to 230 °C. After 30 min, 1.5 mL of saturated TOP-S (2.2 M) stock solution was slowly injected, and the solution was mixed for 40 min at 230 °C. Finally, the zinc precursor stock solution (1 g of $Zn(St)_2$ in 4 mL of ODE) was injected at 230 °C, then the temperature was raised to 260 °C, and mixed for 30 min. At the end of the reaction, the temperature of crude solution was cooled down. For the centrifugation process, a small amount of hexane was added to the as-synthesized Cu:InP/ZnSe/ZnS QD crude solution and centrifuged at 11,000 rpm for 3 min to minimize the zinc precursor impurity in the main solution as mentioned before. To precipitate the Cu:InP/ZnSe/ZnS core/shell/shell QDs, ethanol was used. The centrifugation process was repeated two times using hexane-ethanol. Cu:InP/ZnSe/ZnS QDs were suspended in chloroform for LSC fabrication.

2.7 The fabrication of the QD-based liquid LSC

Cu:InP/ZnSe/ZnS QDs synthesized in chloroform were dispersed in paraffin oil at varying concentrations. Polydimethylsiloxane (PDMS) and a curing agent (CA) were mixed in a 5:1 mass ratio and vigorously stirred for 5 min to ensure homogeneity. The mixture was then degassed in a vacuum desiccator for 1 h to remove air bubbles. A thin PDMS film (100 μm) was created on a 5 cm × 5 cm × 0.2 cm glass substrate using the doctor-blade technique and cured at 120 °C for 1 h. A ultraviolet (UV)-polymerization technique was employed to fabricate a PDMS spacer and a top layer, defining a cavity for the QD solution. The mold was exposed to UV light for 1 h to complete the photopolymerization process. Finally, the liquid LSC was assembled by injecting the QD solution into the cavity. The resulting LSC dimensions were 5 cm × 5 cm × 0.7 cm, with an active area of 4 cm × 4 cm × 0.3 cm.

2.8 Optical characterization of QDs

The UV/visible absorption and photoluminescence (PL) spectra of QDs were carried out by the FS5 spectrofluorometer and FLS1000 fluorescence spectrometer from Edinburgh Instruments, respectively. The FS5 spectrofluorometer included a 150 W xenon lamp combined with an excitation monochromator. The excitation

wavelength was 375 nm. For the emission measurements by the FLS1000 fluorescence spectrometer, the excitation source was a 450 W ozone free xenon arc lamp that covered a range of 230 to > 1000 nm. The emission range was adjusted between 600 and 1400 nm. The samples were excited with 450 nm wavelength. To measure the absorption and PL emission, as-synthesized core/shell QDs were poured into standard quartz cuvettes. The PLQY measurements were performed using the FLS1000 fluorescence spectrometer equipped with an integrating sphere, exciting at 610 nm using the output of Xe lamp. For the absorption spectra of the QD-LSC samples, the SHIMADZU UV-3600 UV-VIS-NIR spectrophotometer was used. For the PL spectra and PLQY calculation of the QD-LSC samples, the FLS1000 fluorescence spectrometer was used. The emission range was adjusted between 600 and 1400 nm. For the PLQY calculation of QD-LSC devices, the excitation wavelength was 610 nm. Time-resolved PL measurements of the Cu:InP/ZnSe/ZnS QDs were performed by using the Picoquant MicroTime 100 time-resolved confocal fluorescence microscope. A picosecond diode laser (λ_{exc} = 375 nm) at a repetition rate of 60 MHz coupled to a 40× objective lens was used as an excitation beam. Bandpass filters with a bandwidth of 15 nm were utilized for spectrally resolved data. All the time-resolved lifetime measurements were performed at room temperature.

2.9 Structural characterization of QDs

Small angle X-ray scattering (SAXS) experiments were performed with the SAXSpoint 5.0 instrument equipped with the Primux 100 copper source having a copper anode with an emission wavelength of 1.5418 Å for Kα and the Eiger2 R 1M horizontal detector from Anton Paar. The distances from the sample to detector in measurements were 1603 and 500 mm for SAXS and medium angle X-ray scattering (MAXS) analyses, respectively. In the scattering graphs, the intensity profiles were given as a function of the scattering vector (q, nm^{-1}), which has a correlation seen in Bragg equation with $q = (4\pi/\lambda)\sin(2\theta/2)$, where 2θ is the scattering angle. Samples were prepared in n-hexane and the tube cell sample holder was used to prevent any leaks from the system. The duration of the measurements was 600 s for each sample, and the background and the scattering data after the n-hexane background subtraction were obtained. The data reduction was performed using the software program SAXS Analysis. Extracted data was fitted using SASView program, version 6.0.0, and *ab initio* model was obtained by BioXTAS RAW 2.3.0 program using DENSS tool.

High resolution transmission electron microscopy (HRTEM) images were recorded using FEI TALOS F200S TEM electron microscope operated at an accelerating voltage of 200 kV. Samples for TEM were prepared on 300-mesh carbon coated Cu grids. Cu-doped InP/ZnSe/ZnS QDs dissolved in hexane were drop-cast on Cu-grids and dried.

X-ray diffraction (XRD) of Cu:InP/ZnSe/ZnS QDs was carried out using a Rigaku Miniflex XRD ($\lambda_{Cu\ K\alpha}$ = 1.54 Å) with a scan rate of 5°·min^{-1}. XRD samples were prepared by drop-casting QDs dissolved in hexane onto 1 cm × 1 cm silicon wafers and heated to 100 °C, and kept at this temperature for 1 h to dry liquid QDs on the silicon wafers. XRD measurements were carried out at room temperature.

For the X-ray photoelectron spectroscopy (XPS) measurement, the same sample preparation method was followed. XPS measurements were performed using a Thermo Scientific K-α (Al Kα source) surface analysis tool at ultrahigh vacuum conditions. For the analysis, binding energies in the XPS data were calibrated with reference to the C–C bond in the C 1s spectrum (284.6 eV).

3 Results and discussion

3.1 Structure of QDs

A one-pot synthesis scheme was developed for SWIR-emitting Cu:InP/ZnSe/ZnS core/shell/shell QDs (Fig. 2). InP core QDs were synthesized using an amine-derived approach [14, 39], which involves reacting indium and zinc halides in a primary amine coordinating solvent (i.e., OAm). $(DEA)_3P$, a cost-effective, safe, and highly stable phosphine precursor [40, 41], was selected to facilitate the synthesis of InP nanocrystals under ambient conditions. $InCl_3$, which promotes the formation of larger QDs [14], was mixed with OAm, whereas the commonly used $ZnCl_2$ was excluded from the reaction due to its restriction on the growth of InP cores (Fig. 1(b)). The solution was degassed at 120 °C for 2 h, then heated to 200 °C under an argon atmosphere. Subsequently, a $(DEA)_3P$ solution was rapidly injected, resulting in the formation of InP QDs. Considering the strong reactivity of copper ions with phosphorus atoms, the copper stearate was introduced after the InP formation to eliminate the possible $Cu_{3-x}P$ phases in the crystal structure that can lead to blue shift of emission [42, 43]. Then, the epitaxial growth of the ZnSe inner shell with a relatively lower lattice mismatch (3.4%) and ZnS outer shell (7.6%) yielded efficient Cu:InP/ZnSe/ZnS QDs.

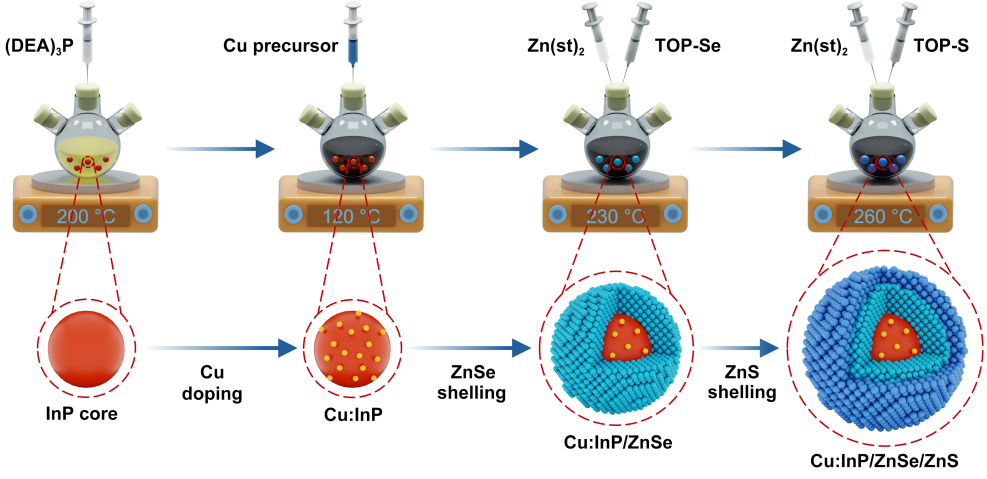


Figure 2 Schematic of the synthesis route for multishell Cu:InP/ZnSe/ZnS QDs.

Figures 3(a)–3(d) depict representative bright field transmission electron microscopy (TEM) images of Cu:InP/ZnSe/ZnS core/shell/shell QDs at each synthesis stage. As illustrated in Fig. 3(a), the synthesized InP core QDs exhibited an average diameter of 3.4 ± 0.5 nm. Upon introducing copper dopant at a Cu:In ratio of 0.05, QDs experienced a modest increase in size to 3.6 ± 0.5 nm (Fig. 3(b)). The XPS analysis of Cu:InP/ZnSe/ZnS QDs (Figs. S1 and S2 in the ESM) revealed distinct photoelectron signals attributed to Cu $2p_{3/2}$ and Cu $2p_{1/2}$, located at 931.68 and 951.68 eV, respectively (Fig. 3(e)). Subsequent growth of ZnSe inner and ZnS outer shells resulted in further size enlargement to 4.3 ± 0.6 and 5.4 ± 0.7 nm, respectively, while they show a spherical morphology and uniform size distribution (Figs. S3 and S7 in the ESM).

To further investigate the crystal structure and the morphology of the synthesized QDs, X-ray diffraction (XRD) patterns were measured for both undoped InP cores and Cu-doped InP/ZnSe/ZnS core/shell/shell QDs (Fig. 3(f)). A comparison of the XRD patterns revealed that the three primary reflection peaks observed at 26.94°, 44.42°, and 52.57° correspond to the (111), (220), and (311) planes of the InP cores, respectively, which are in agreement with the InP phase (PDF card No: 1538801), exhibiting a slight shift to higher angles upon Cu-doping. This shift indicates the successful incorporation of Cu into the InP core crystal lattice. Subsequent growth of the ZnSe inner shell and ZnS outer shell on the Cu-doped InP cores resulted in a more pronounced shift of these reflection peaks towards the positions characteristic of the ZnSe (PDF card No. 1538613) and ZnS (PDF card No. 1539414) phases, respectively. No additional peaks were observed, confirming the absence of secondary phase formation and the successful growth of the ZnSe and ZnS shell materials. During the doping and shell growth stages, the observed peak narrowing, a consequence of crystal size enlargement, confirms the epitaxial growth on the InP core. This growth process is consistent with preserving the zinc-blende crystalline structure of the InP core. The average particle size, as calculated by the Scherrer equation, correlates well with the TEM analysis (Eq. (S1) in the ESM).

The QD nanostructures were further analyzed using SAXS. The SAXS intensity profile as a function of the scattering vector is shown in Fig. 3(g). According to these profiles, at lower q values, a flattened Guinier plateau can be seen for QDs except for the InP core due to the slightly distinct shape and possible aggregation of the core. Table S2 in the ESM shows the K values extracted from the slope of the low q values using power law slopes, which proves the transition from the elongated to spherical shapes. In addition, the pair distance distribution function (PDDF) graphs (Fig. S4 in

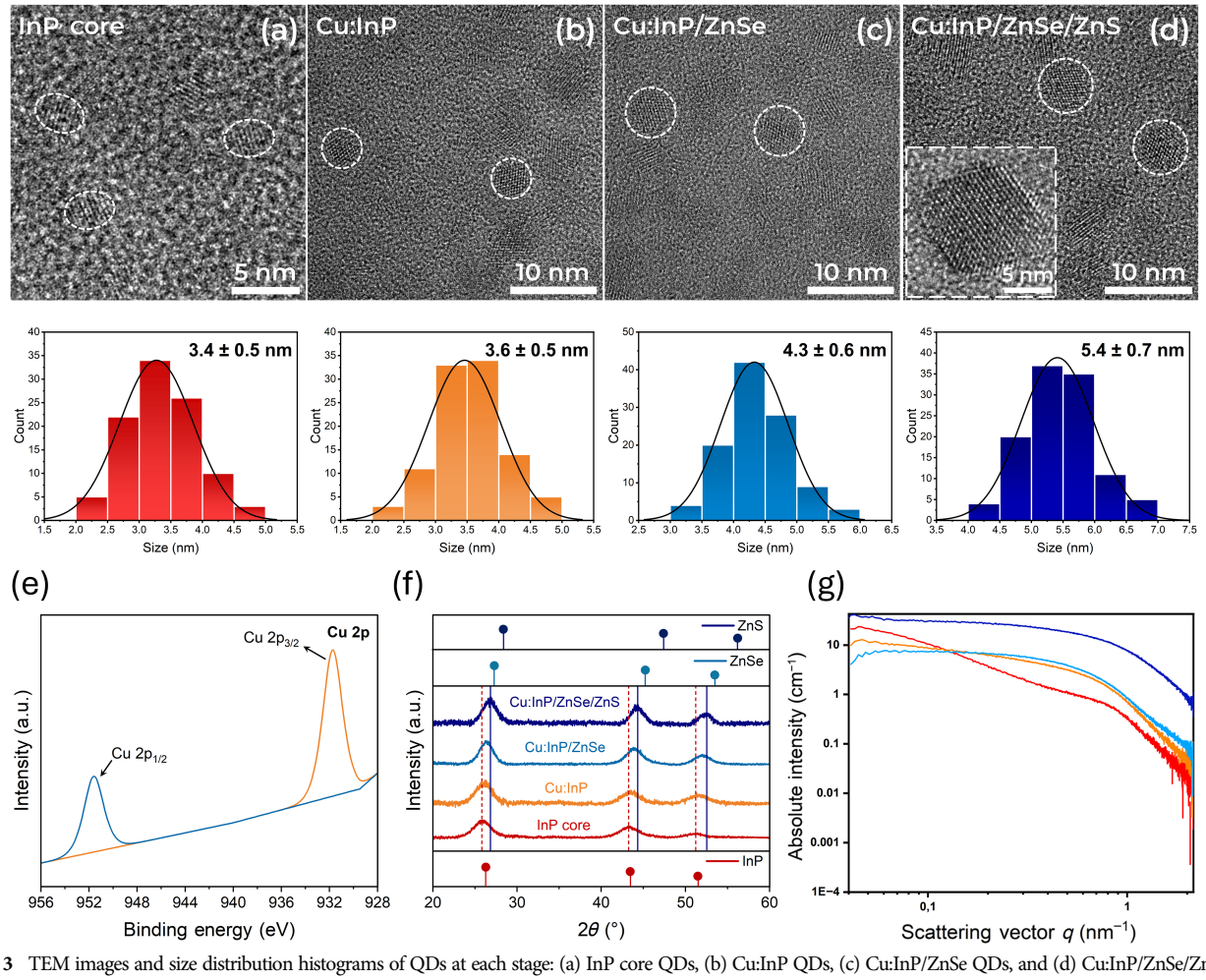


Figure 3 TEM images and size distribution histograms of QDs at each stage: (a) InP core QDs, (b) Cu:InP QDs, (c) Cu:InP/ZnSe QDs, and (d) Cu:InP/ZnSe/ZnS QDs with an HRTEM image (bottom-left). (e) XPS spectrum of Cu 2p core levels in Cu:InP QDs. (f) XRD patterns of undoped InP core (PDF card No. 1538801), Cu:InP (Cu:In ratio of 0.05), Cu:InP/ZnSe (PDF card No. 1538613), and Cu:InP/ZnSe/ZnS QDs (PDF card No. 1539414). (g) SAXS graphs of the InP core (red), Cu:InP (orange), Cu:InP/ZnSe (light blue), and Cu:InP/ZnSe/ZnS (dark blue) QDs.

the ESM), which indicate the distribution of distances between individual particles in the sample volume and reflect the average particle dimensions [44], were derived from the scattering profiles of these samples by SASView software using the inversion tool. According to the bell-like PDDF graphs, all QDs have a spherical shape. For the InP core, it is seen in Table S2 in the ESM that the *K* value for the Guinier region is close to −1, which indicates a little distortion from the symmetric spherical geometry and has a rather elongated shape, giving it a rod-like structure. Moreover, after Cu-doping, the core adopts a more homogeneous and symmetrical structure, as evidenced by a decrease in power-law-*K*-values from −0.95 for InP core to −0.45 with a high polydispersity ratio (0.97), and a sharper and smoother interface was observed with a decreased Porod slope of q = −3.79 (Fig. S5 and Table S2 in the ESM). The Porod region is characterized by higher q values in SAXS graphs and is correlated to the smoothness of the surface of particles by its slope. The growth of the ZnSe and ZnS shells further enhances the sphericity and increases the particle size with a smoother surface. Furthermore, the SAXS-derived average radius for the QDs, depending on the electron density differences, was calculated via the Levenberg–Marquardt fitting optimizer model in SASView software and showed strong agreement with TEM measurements, yielding a radius of Gyration of ~ 1.83, ~ 1.87, ~ 2.24, and ~ 2.86 nm for the InP core, Cu:InP, Cu:InP/ZnSe core/shell, and Cu:InP/ZnSe/ZnS core/shell/shell QDs, respectively. Lastly, the *ab initio* model of Cu:InP/ZnSe/ZnS core/shell/shell QDs was calculated using DENSS on BioXTAS RAW program (Fig. S7 in the ESM) and it provided a consistent model with the TEM image of the synthesized QDs [45].

3.2 Optical properties of QDs

Undoped InP core QDs exhibited a sharp excitonic absorption peak at 696 nm without any emission (Fig. 4(a)). The copper doping introduces hole acceptor states within the bandgap, enabling radiative recombination of photo-generated holes at the Cu dopant level with electrons from the conduction band of InP (Fig. 4(b)) [46–48]. This results in a red-shifted PL emission. We systematically investigated the influence of Cu doping concentration by synthesizing Cu:InP QDs with Cu/In ratios of 0.01, 0.025, 0.05, and 0.1. At lower ratios (0.01 and 0.025),

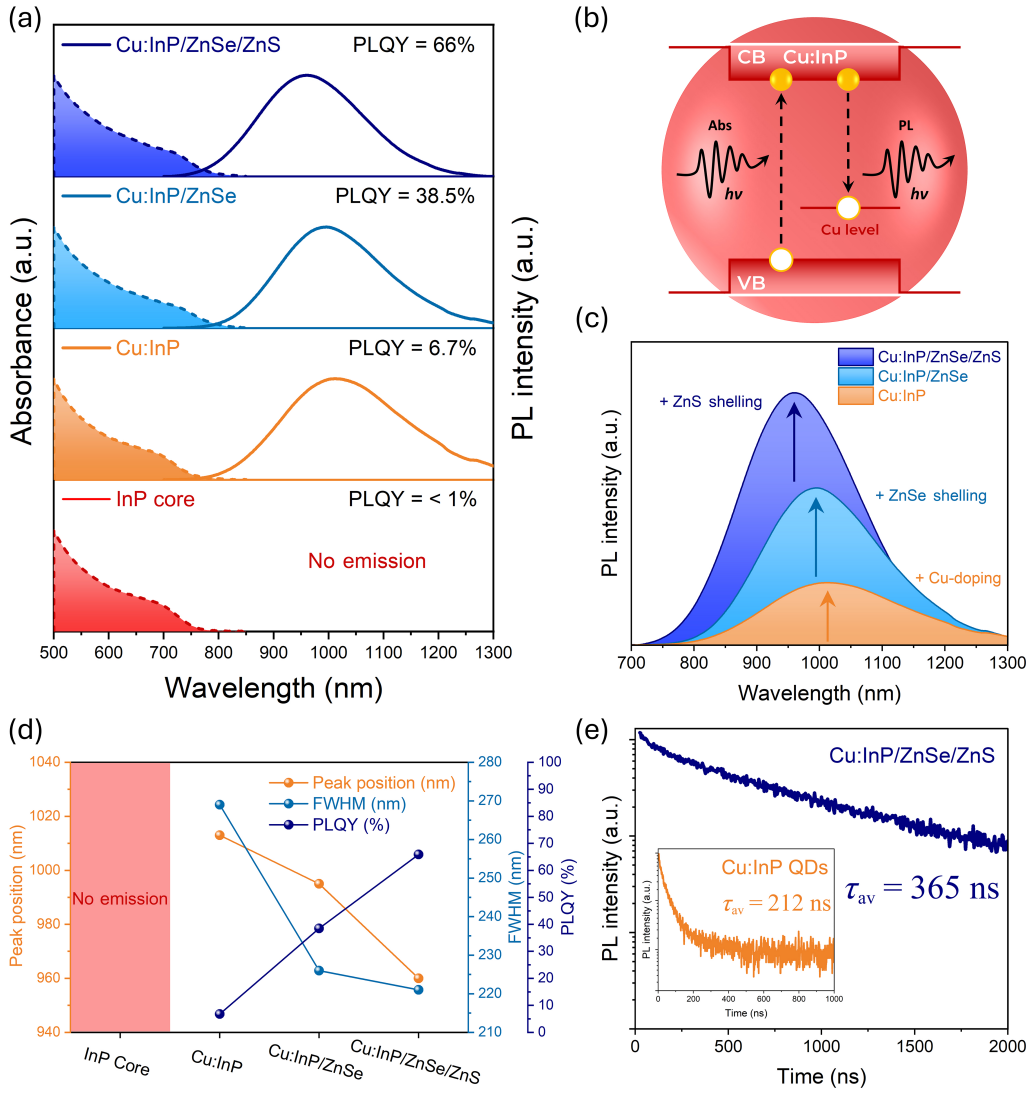


Figure 4 (a) Absorbance and PL spectra of InP core, Cu:InP, Cu:InP/ZnSe, and Cu:InP/ZnSe/ZnS QDs. (b) Energy band diagram of Cu:InP nanocrystals showing mid-gap states from copper doping, enabling SWIR emission. (c) PL intensity profiles of QDs at different synthesis stages. (d) Evolution of PL peak wavelength, FWHM, and PLQY during the synthesis process (Table S3 in the ESM). (e) Time-resolved PL (TRPL) decay profiles of Cu:InP and Cu:InP/ZnSe/ZnS QDs.

insufficient Cu doping failed to passivate surface traps, resulting in no detectable emission (Fig. S8 in the ESM). For Cu:InP QDs synthesized with a Cu:In ratio of 0.05, a prominent PL peak was observed at 1013 nm with a full width at half maximum (FWHM) of 269 nm and a PLQY of 6.7%. The improvement in PLQY is attributed to the passivation of surface defects by the Cu ions, which arises from the passivation of the nonradiative surface traps, resulting in the structural relaxation around the Cu sites and photogenerated hole localization [10, 31]. However, the relatively low PLQY of 6.7% suggests the presence of carrier trapping at the surface of the QDs [42]. Further increasing Cu concentration led to a red shift in the PL emission, consistent with prior reports [49]. However, excessive doping (Cu/In = 0.1) reduced the PLQY, likely due to the formation of hole scattering centers that disrupt the photoexcited carrier transfer process (Fig. S7 in the ESM) [48].

To further enhance the optical properties, a core/shell/shell structure was grown on the Cu:InP QDs. The growth of an initial 0.7 nm ZnSe inner shell resulted in a slight blue shift of the PL emission peak from 1013 (Cu:InP) to 995 nm (Cu:InP/ZnSe), accompanied by a significant increase in PLQY to 38.5%. The lattice-matched ZnSe shell led to narrower and more symmetric XRD peaks (Fig. 3(f)) and improved sphericity/surface smoothness (Figs. 3(a)–3(d) and 3(g)). This correlates with a narrower FWHM of photoluminescence (i.e., 226 nm), suggesting suppressed inhomogeneous emission broadening compared to Cu:InP core QDs. Subsequent growth of a 1.1 nm ZnS outer shell (bandgap of 3.68 eV) further improved the optical properties, resulting in a PL emission peak at 960 nm, a PLQY of 66%, and a reduced FWHM of 221 nm (Fig. 4(d) and Table S3 in the ESM). Because the non-radiative channels were passivated by shell growth, the final Cu:InP/ZnSe/ZnS QD nanostructure demonstrated a significantly prolonged PL decay profile with an extended average lifetime of 365 ns (Eq. (S2) and Table S4 in the ESM) in comparison with Cu:InP core QDs with a lifetime of 212 ns (Fig. 4(e)). Control experiments with $ZnCl_2$ yielded QDs with notably shorter emission (peaking at 856 nm), which indicates the importance of removing it for SWIR emission (Fig. S9 in the ESM).

Although $ZnCl_2$ is commonly introduced in aminophosphine-based InP QD syntheses because its presence effectively narrows the size distribution and enhances photoluminescence properties [14, 50], the main distinction of our synthetic strategy lies in the elimination of the zinc halide source ($ZnCl_2$) from the reaction environment. To compensate for the absence of $ZnCl_2$, we employed a cost-effective aminophosphine precursor, tris(diethylamino)phosphine, which facilitated a balanced In:P stoichiometry [25] and stabilized early-stage nucleation, thereby minimizing surface defects and maintaining high PLQY [51]. Notably, although the omission of $ZnCl_2$ in related III–V systems such as InAs/ZnSe QDs leads to a drastic decrease in PLQY (from ~ 70% to 10%–20%) due to insufficient surface passivation and uncontrolled reaction kinetics [52], the InP system inherently exhibits more stable indium- and phosphorus-terminated surfaces capable of sustaining efficient luminescence [25]. Finally, the epitaxial growth of a lattice-matched ZnSe/ZnS multishell further suppressed nonradiative recombination [20], resulting in highly efficient red-to-SWIR Cu-doped InP QDs.

3.3 LSC performance

To fabricate Cu:InP/ZnSe/ZnS QD-based liquid LSCs, we designed a structural configuration using a solid-state PDMS polymer as a light-guiding layer to form a cavity that houses the QD solution, serving as the luminescent interlayer (Fig. 5). The liquid QD integration preserves PLQY and spectral properties (Figs. S10 and S11 in the ESM), whereas the solid-state incorporation can induce host material effects, reducing PLQY and causing unwanted spectral shifts [53, 54]. Efficient light-to-electricity conversion requires maintaining the light-guiding properties of the QD medium to the solar cells. To achieve this, the refractive index (RI) of the QD solution must be closer to the surrounding material while preserving high optical performance in the liquid state [55]. To meet these criteria, we dispersed QDs in transparent paraffin oil (RI = 1.47), and although their PLQY was 66% in hexane, it exhibited only a minimal drop to 52% in paraffin oil, ensuring efficient spontaneous emission.

The fabrication process involved three main steps (Fig. 5). First, a thin polymer sheet (100 μm) was formed using the doctor-blade technique, a well-established method for producing uniform layers [56]. PDMS was chosen as the transparent, lower index cladding layer (RI = 1.46) for the liquid QD medium [32]. Second, PDMS spacers were applied along the sheet edges using optical adhesive to contain the liquid, confining the QD solution while ensuring waveguiding properties. Third, another identical polymer sheet was affixed to the spacers, creating a sealed cavity. The Cu:InP/ZnSe/ZnS QD solution was then injected into the central

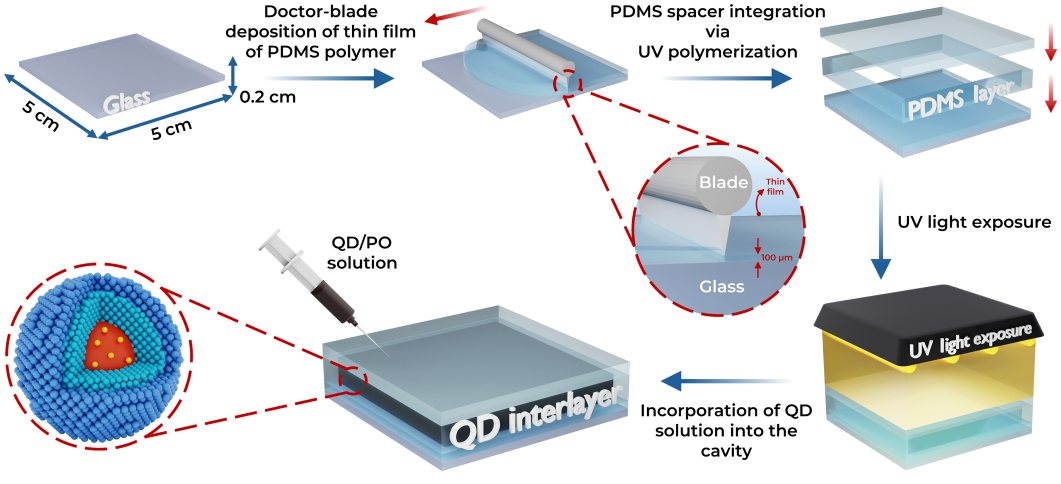


Figure 5 Schematic of the fabrication process for QD-based liquid LSCs.

hollow space (4 cm × 4 cm × 0.3 cm), resulting in a final QD-based liquid LSC structure (5 cm × 5 cm × 0.7 cm).

The overall optical quantum efficiency of an LSC is directly linked to its absorption and internal collection efficiencies, with the latter being directly proportional to the PLQY of the QDs. Efficient LSCs require QDs with broad absorption spectra, a large Stokes shift to minimize self-absorption, and an optimized emission spectrum that matches the solar cell's spectral response [57–59]. To evaluate the electro-optical performance of the Cu:InP/ZnSe/ZnS QD-based liquid LSC, one edge of the fabricated device was coupled to a commercial Si-based solar cell, whereas the remaining edges were covered with black tape to minimize unwanted light reflection [60]. With a geometric factor (G) of 1.42, the device was illuminated perpendicularly under a standard AM 1.5G solar radiation (Fig. S12 in the ESM). The electro-optical efficiency (η_{opt}) was determined by using Eq. (1)

$$\eta_{opt} = \frac{I_{SC}^{LSC}}{I_{SC}^{PV} \times G} \quad (1)$$

where I_{SC}^{PV} represents the short-circuit current of a Si photovoltaic (PV) cell under direct solar illumination, I_{SC}^{LSC} shows the short-circuit current of a Si PV cell with the LSC under direct solar illumination, and G accounts for the ratio of the LSC's top surface area to the total edge surface area.

The optical efficiency of the QD-based liquid LSCs is highly dependent on QD concentration (Fig. 6(a)). At 7 mg·mL^{-1}, an optical efficiency of 4.79% was achieved, attributed to the high PLQY of 52% within the device (Fig. 6(b)). This value closely aligns with the theoretical estimate ($\eta_{opt} = \eta_{abs} \times \eta_{int}$, where η_{abs} = 14.23% and η_{int} = 35.73%), yielding a theoretical efficiency of 5.08% (Eqs. (S3)–(S7) in the ESM). The deviation between experimental and simulated results is possibly due to the imperfect coupling of edge-emitted light into the photovoltaic cells [57]. Additionally, at this concentration, the device exhibited an average visible transmittance (AVT) (Eq. (S8) in the ESM) over 68% (Fig. 6(c)). Figure 6(d) highlights the LSC's optical clarity and color fidelity under ambient lighting, corroborating its spectral transmittance profile.

Increasing the QD concentration to 14 mg·mL^{-1} enhanced the optical efficiency to 5.36% due to increased light absorption, though the PLQY dropped to 34.7%. This increase in QD density led to a reduction in AVT to 42.7% due to stronger absorption. At 27 mg·mL^{-1}, the highest optical efficiency of 7.36% was recorded, whereas PLQY declining to 32.8%. However, at 50 mg·mL^{-1}, the efficiency declined despite higher absorption, as PLQY dropped to 25.9%. The diminishing PLQY at higher concentrations introduced energy losses that outweighed contributions by the relatively higher absorption, ultimately reducing performance. Nevertheless, despite the significantly reduced AVT at 50 mg·mL^{-1}, the proposed concentration could still serve as a partially transmitting "luminescent solar curtain" in regions with high solar irradiance, where the intense light compensates for lower transparency while enabling substantial energy harvesting [61].

Furthermore, incorporating the QDs with an emission wavelength in the range of 900–1000 nm, which aligns with the spectral responsivity of silicon solar cells, can substantially enhance power conversion efficiency (PCE) (Eq. (S10) in the ESM), which serves as a key performance metric for QD-based LSCs (Fig. 6(e)). By combining measured optical efficiency with coupling efficiency to the Si PV cell, the PCE at 7 mg·mL^{-1} was found to be 0.1%. As QD concentration increased to 27 mg·mL^{-1}, PCE rose to 0.18%, reflecting greater light-harvesting potential. The photostability of the LSC was evaluated under high-intensity UV illumination (~ 1.3 W·cm^{-2}, equivalent to 260-sun illumination) at room temperature. After 7 h of continuous exposure, the PL intensity retained approximately 65% of its initial value (Fig. 6(f)). Paraffin oil, with its low volatility and high thermal stability, mitigates solvent evaporation and provides a protective matrix for the QDs. Additionally, the high refractive index of paraffin oil (~ 1.47) improves light trapping within the LSC, further enhancing its optical efficiency.

4 Conclusions

In this study, we synthesized highly efficient Cu-doped InP/ZnSe/ZnS QDs with SWIR emission. By employing a safe and stable $(DEA)_3P$ precursor and omitting $ZnCl_2$, a significant red shift in the absorbance of the InP core was observed. Subsequent Cu doping resulted in an emission peak at 1013 nm, a prolonged lifetime, and an improved PLQY to ~ 7%. The epitaxial growth of a ZnSe/ZnS multishell structure further enhanced the PLQY to 66% with an emission peak at 960 nm.

The integration of these QDs into a liquid-based LSC facilitated a high optical efficiency of 7.36%. This performance was enabled by (1) their exceptional PLQY, (2) spectral alignment with the responsivity peak of silicon solar cells, and (3) core/cladding waveguide structure. Our findings highlight the promise of Cu-doped InP QDs as an eco-friendly nanomaterial for SWIR emission, with significant implications for applications such as bioimaging, biosensors, and next-generation luminescent solar concentrators. This work not only advances the field of InP-based QDs but also opens new avenues for high-performance infrared optoelectronics.

Electronic Supplementary Material: Supplementary material (details of the QD synthesis, fabrication of the QD-based liquid LSC, optical and structural characterizations (the Experimental section); summary of key optical properties of InP QDs from selected previous reports (Table S1); XPS measurements (Figs. S1 and S2); TEM measurements (Fig. S3); Scherrer equation (Eq. (S1)); PDDF graphs (Fig. S4); MAXS measurements (Fig. S5); results of K values upon fitting on different regions of SAXS graphs (Table S2); additional SAXS measurements (Fig. S6); *ab initio* bead models (Fig. S7); Cu dependent PL properties (Fig. S8); average PL lifetime formula (Eq. (S2)); PL parameters for QD samples (Table S3); $ZnCl_2$ dependent PL spectra (Fig. S9); parameters of the PL decays (Table S4); absorbance and PL spectra for QD samples (Fig. S10–S12); LSC performance metrics (Eqs. (S3)–(S10)); and references) is available in the online version of this article at https://doi.org/10.26599/NR.2025.94908234.

Data availability

All data needed to support the conclusions in the paper are presented in the manuscript and the Electronic Supplementary Material. Additional data related to this paper may be requested from the corresponding author upon request.

Acknowledgements

This work was funded by Berteks Tekstil. The authors gratefully acknowledge Dr. Gulcan Corapcioglu from the Koç University

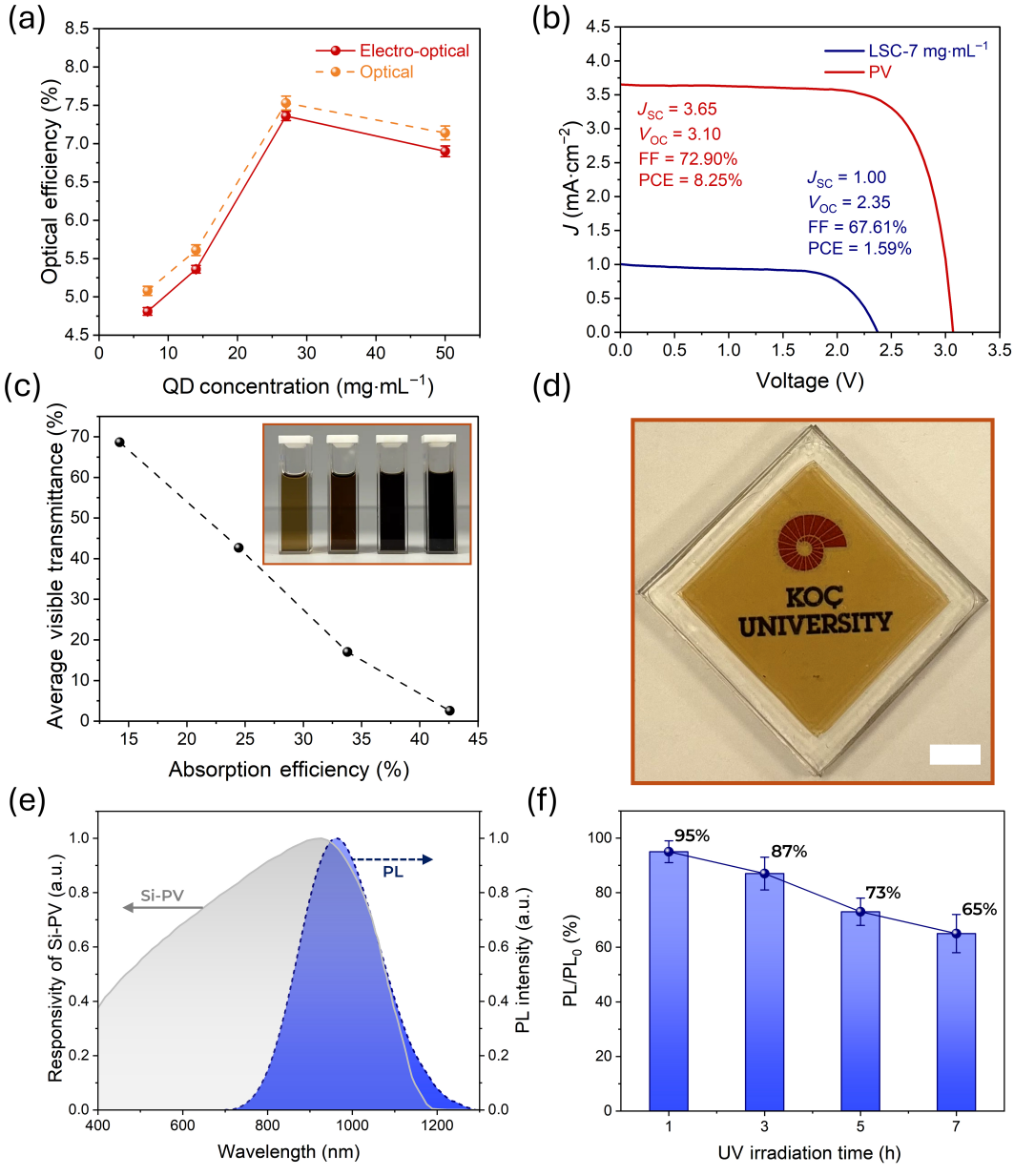


Figure 6 (a) Optical efficiency of QD-based liquid LSCs as a function of QD concentration, measured using electro-optical and optical methods. (b) *J*–*V* characteristics of a silicon solar cell measured under two conditions: (red) standalone PV (without LSC) and (blue) integrated with a QD-based LSC (QD concentration: 7 mg·mL^{-1}) under AM 1.5G illumination. The short-circuit current density was determined by dividing the area of the Si solar cell. To account for the total LSC performance, given that only one side of the LSC interfaces with the solar cell in the measurement setup, the current density was then multiplied by a factor of 4. FF: fill factor. (c) Average visible transmittance (%) and absorption efficiency (%) of Cu:InP/ZnSe/ZnS QD solutions with concentrations ranging from 7 to 50 mg·mL^{-1} (left to right). Inset: photograph of the QD solutions in a typical cuvette under ambient light. (d) Photograph of a QD-based liquid LSC under ambient light (scale bar = 1 cm). (e) Normalized PL output of the fabricated QD-based LSCs (QD concentration: 7 mg·mL^{-1}), with the grey-shaded spectrum representing the responsivity of Si-PV. (f) Photostability of LSCs under UV irradiation, showing normalized PL intensity (PL/PL$_0$) after 7 h, where PL$_0$ is the initial and PL the final emission integral.

Nanofabrication and Nanocharacterization Center for Scientific and Technological Advanced Research for providing TEM and HRTEM imaging. We also extend our thanks to Suleyman Tekmen for his assistance in HRTEM characterization. The authors are grateful to Dr. Barış Yagcı from the Koç University Surface Science and Technology Center (KUYTAM) for performing the XPS measurements. Additionally, we thank the Koç University Boron and Advanced Materials Application and Research Center (KUBAM) for conducting the XRD analysis. The authors extend their gratitude to Sevgi Döndü Özen for her valuable assistance in preparing the revised manuscript.

Declaration of competing interest

All the contributing authors report no conflict of interests in this work.

Author contribution statement

T. S. K.: Conceptualization, methodology, software, validation, formal analysis, investigation, data curation, writing – original draft, writing – review & editing, visualization. U. B. C.: Software, validation, formal analysis, data curation, writing – original draft,

writing – review & editing. P. K.: Formal analysis, data curation. A. O.: Methodology, formal analysis. E. T.: Validation, formal analysis. G. O. E.: Methodology, validation. H. G.: Methodology, software, validation, formal analysis, data curation, writing – original draft, writing – review & editing, visualization. H. J.: Software, validation, data curation. M. S.: Funding acquisition, investigation. K. K.: Funding acquisition, investigation. U. U.: Software, investigation. S. N.: Conceptualization, investigation, resources, writing – original draft, writing – review & editing, supervision, project administration, funding acquisition. All authors have approved the final version of the manuscript.

Use of AI statement

None.

References

[1] Brus, L. E. Electron–electron and electron–hole interactions in small semiconductor crystallites: The size dependence of the lowest excited electronic state. *J. Chem. Phys.* **1984**, *80*, 4403–4409.

[2] Norris, D. J.; Bawendi, M. G. Measurement and assignment of the size-dependent optical spectrum in CdSe quantum dots. *Phys. Rev. B* **1996**, *53*, 16338–16346.

[3] Flatae, A. M.; Tantussi, F.; Messina, G. C.; De Angelis, F.; Agio, M. Plasmon-assisted suppression of surface trap states and enhanced band-edge emission in a bare CdTe quantum dot. *J. Phys. Chem. Lett.* **2019**, *10*, 2874–2878.

[4] Mallem, K.; Prodanov, M. F.; Chen, D. Z.; Marus, M.; Kang, C. B.; Shivarudraiah, S. B.; Vashchenko, V. V.; Halpert, J. E. Solution-processed red, green, and blue quantum rod light-emitting diodes. *ACS Appl. Mater. Interfaces* **2022**, *14*, 18723–18735.

[5] Guzelturk, B.; Diroll, B. T.; Cassidy, J. P.; Harankahage, D.; Hua, M. C.; Lin, X. M.; Iyer, V.; Schaller, R. D.; Lawrie, B. J.; Zamkov, M. Bright and durable scintillation from colloidal quantum shells. *Nat. Commun.* **2024**, *15*, 4274.

[6] Haque, A.; Zhu, T.; Tounesi, R.; Lee, S.; Vafaie, M.; Huerta Hernandez, L.; Davaasuren, B.; Genovese, A.; Sargent, E. H.; Baran, D. Electrical tunability of quantum-dot-in-perovskite solids. *ACS Nano* **2024**, *18*, 34089–34095.

[7] Liao, Z. B.; Mallem, K.; Prodanov, M. F.; Kang, C. B.; Gao, Y. Y.; Song, J. X.; Vashchenko, V. V.; Srivastava, A. K. Ultralow roll-off quantum dot light-emitting diodes using engineered carrier injection layer. *Adv. Mater.* **2023**, *35*, 2303950.

[8] Chen, B.; Li, D. Y.; Wang, F. InP quantum dots: Synthesis and lighting applications. *Small* **2020**, *16*, 2002454.

[9] Karadza, B.; Schiettecatte, P.; Van Avermaet, H.; Mingabudinova, L.; Giordano, L.; Respekta, D.; Deng, Y. H.; Nakonechnyi, I.; De Nolf, K.; Walravens, W. et al. Bridging the green gap: Monochromatic InP-based quantum-dot-on-chip LEDs with over 50% color conversion efficiency. *Nano Lett.* **2023**, *23*, 5490–5496.

[10] Almeida, G.; Ubbink, R. F.; Stam, M.; Du Fossé, I.; Houtepen, A. J. InP colloidal quantum dots for visible and near-infrared photonics. *Nat. Rev. Mater.* **2023**, *8*, 742–758.

[11] Cros-Gagneux, A.; Delpech, F.; Nayral, C.; Cornejo, A.; Coppel, Y.; Chaudret, B. Surface chemistry of InP quantum dots: A comprehensive study. *J. Am. Chem. Soc.* **2010**, *132*, 18147–18157.

[12] Yu, P.; Shan, Y. L.; Cao, S.; Hu, Y. Q.; Li, Q. Y.; Zeng, R. S.; Zou, B. S.; Wang, Y. J.; Zhao, J. L. Inorganic solid phosphorus precursor of sodium phosphaethynolate for synthesis of highly luminescent InP-based quantum dots. *ACS Energy Lett.* **2021**, *6*, 2697–2703.

[13] Kim, T. G.; Zherebetskyy, D.; Bekenstein, Y.; Oh, M. H.; Wang, L. W.; Jang, E.; Alivisatos, A. P. Trap passivation in indium-based quantum dots through surface fluorination: Mechanism and applications. *ACS Nano* **2018**, *12*, 11529–11540.

[14] Tessier, M. D.; Dupont, D.; De Nolf, K.; De Roo, J.; Hens, Z. Economic and size-tunable synthesis of InP/ZnE (E = S, Se) colloidal quantum dots. *Chem. Mater.* **2015**, *27*, 4893–4898.

[15] Reid, K. R.; Mcbride, J. R.; Freymeyer, N. J.; Thal, L. B.; Rosenthal, S. J. Chemical structure, ensemble and single-particle spectroscopy of thick-shell InP-ZnSe quantum dots. *Nano Lett.* **2018**, *18*, 709–716.

[16] Bang, E.; Choi, Y.; Cho, J.; Suh, Y. H.; Ban, H. W.; Son, J. S.; Park, J. Large-scale synthesis of highly luminescent InP@ZnS quantum dots using elemental phosphorus precursor. *Chem. Mater.* **2017**, *29*, 4236–4243.

[17] Pu, Y. C.; Fan, H. C.; Chang, J. C.; Chen, Y. H.; Tseng, S. W. Effects of interfacial oxidative layer removal on charge carrier recombination dynamics in InP/$ZnSe_xS_{1-x}$ core/shell quantum dots. *J. Phys. Chem. Lett.* **2021**, *12*, 7194–7200.

[18] Pietra, F.; De Trizio, L.; Hoekstra, A. W.; Renaud, N.; Prato, M.; Grozema, F. C.; Baesjou, P. J.; Koole, R.; Manna, L.; Houtepen, A. J. Tuning the lattice parameter of In_xZn_yP for highly luminescent lattice-matched core/shell quantum dots. *ACS Nano* **2016**, *10*, 4754–4762.

[19] Hughes, K. E.; Stein, J. L.; Friedfeld, M. R.; Cossairt, B. M.; Gamelin, D. R. Effects of surface chemistry on the photophysics of colloidal InP nanocrystals. *ACS Nano* **2019**, *13*, 14198–14207.

[20] Li, Y.; Hou, X. Q.; Dai, X. L.; Yao, Z. L.; Lv, L. L.; Jin, Y. Z.; Peng, X. G. Stoichiometry-controlled InP-based quantum dots: Synthesis, photoluminescence, and electroluminescence. *J. Am. Chem. Soc.* **2019**, *141*, 6448–6452.

[21] Won, Y. H.; Cho, O.; Kim, T.; Chung, D. Y.; Kim, T.; Chung, H.; Jang, H.; Lee, J.; Kim, D.; Jang, E. Highly efficient and stable InP/ZnSe/ZnS quantum dot light-emitting diodes. *Nature* **2019**, *575*, 634–638.

[22] Zhao, Y. Y.; Pilvar, A.; Tank, A.; Peterson, H.; Jiang, J.; Aster, J. C.; Dumas, J. P.; Pierce, M. C.; Roblyer, D. Shortwave-infrared meso-patterned imaging enables label-free mapping of tissue water and lipid content. *Nat. Commun.* **2020**, *11*, 5355.

[23] Wang, Y. J.; Wu, H.; Rodà, C.; Peng, L. C.; Taghipour, N.; Dosil, M.; Konstantatos, G. Shortwave infrared light detection and ranging using silver telluride quantum dots. *Adv. Mater.* **2025**, *37*, 2500977.

[24] Levy, M.; Bertram, J. R.; Eller, K. A.; Chatterjee, A.; Nagpal, P. Near-infrared-light-triggered antimicrobial indium phosphide quantum dots. *Angew. Chem., Int. Ed* **2019**, *58*, 11414–11418.

[25] Yadav, R.; Kwon, Y.; Rivaux, C.; Saint-Pierre, C.; Ling, W. L.; Reiss, P. Narrow near-infrared emission from InP QDs synthesized with indium(I) halides and aminophosphine. *J. Am. Chem. Soc.* **2023**, *145*, 5970–5981.

[26] Zhang, W. D.; Duan, X. J.; Tan, Y. Z.; Hao, J. J.; Zhu, H. M.; Wang, Q. Q.; Yang, H. C.; Liu, H. C.; Wang, K.; Wang, Z. W. et al. Giant pyramidal near-infrared InP/ZnS quantum dots with size over 15 nm for cell imaging. *Laser Photonics Rev.* **2024**, *18*, 2400367.

[27] Liu, H.; Shang, G. L.; Ren, C.; Gao, Y.; He, T. C. Photophysical properties of Mn-doped InP/ZnS nanocrystals. *J. Phys. Chem. C* **2021**, *125*, 21748–21753.

[28] Zhang, G. L.; Mei, S. L.; Wei, X.; Wei, C.; Yang, W.; Zhu, J. T.; Zhang, W. L.; Guo, R. Q. Dual-emissive and color-tunable Mn-doped InP/ZnS quantum dots via a growth-doping method. *Nanoscale Res. Lett.* **2018**, *13*, 170.

[29] Yang, W.; He, G. X.; Mei, S. L.; Zhu, J. T.; Zhang, W. L.; Chen, Q. H.; Zhang, G. L.; Guo, R. Q. Controllable synthesis of dual emissive Ag:InP/ZnS quantum dots with high fluorescence quantum yield. *Appl. Surf. Sci.* **2017**, *423*, 686–694.

[30] Eren, G. O.; Onal, A.; Karatum, O.; Jahangiri, H.; Ozer, M. S.; Eroglu, Z.; Sundu, B.; Kaya, L.; Burcak, A. B.; Aydemir, U. et al. Ruthenium-doped InP quantum dots for efficient red emission. *ACS Appl. Nano Mater.* **2023**, *6*, 10044–10053.

[31] Xie, R. G.; Peng, X. G. Synthesis of Cu-doped InP nanocrystals (d-dots) with ZnSe diffusion barrier as efficient and color-tunable NIR emitters. *J. Am. Chem. Soc.* **2009**, *131*, 10645–10651.

[32] Sadeghi, S.; Bahmani Jalali, H.; Srivastava, S. B.; Melikov, R.; Baylam, I.; Sennaroglu, A.; Nizamoglu, S. High-performance, large-area, and ecofriendly luminescent solar concentrators using copper-doped InP quantum dots. *iScience* **2020**, *23*, 101272.
[33] Huang, P.; Liu, X. N.; Liu, X.; Wei, J.; Liu, F. Z.; Li, H. B. One-pot synthesis of Cu:InP multishell quantum dots for near-infrared light-emitting devices. *Nano Res.* **2024**, *17*, 10655–10660.
[34] Lim, M.; Lee, W.; Bang, G.; Lee, W. J.; Park, Y.; Kwon, Y.; Jung, Y.; Kim, S.; Bang, J. Synthesis of far-red- and near-infrared-emitting Cu-doped InP/ZnS (core/shell) quantum dots with controlled doping steps and their surface functionalization for bioconjugation. *Nanoscale* **2019**, *11*, 10463–10471.
[35] Kim, J.; Choi, H. S.; Wedel, A.; Yoon, S. Y.; Jo, J. H.; Kim, H. M.; Han, C. J.; Song, H. J.; Yi, J. M.; Jang, J. S. et al. Highly luminescent near-infrared Cu-doped InP quantum dots with a Zn-Cu-In-S/ZnS double shell scheme. *J. Mater. Chem. C* **2021**, *9*, 4330–4337.
[36] Sadeghi, S.; Bahmani Jalali, H.; Melikov, R.; Ganesh Kumar, B.; Mohammadi Aria, M.; Ow-Yang, C. W.; Nizamoglu, S. Stokes-shift-engineered indium phosphide quantum dots for efficient luminescent solar concentrators. *ACS Appl. Mater. Interfaces* **2018**, *10*, 12975–12982.
[37] Jing, Q.; Meng, X. Y.; Wang, C.; Zhao, H. G. Exciton dynamic in pyramidal InP/ZnSe quantum dots for luminescent solar concentrators. *ACS Appl. Nano Mater.* **2023**, *6*, 4449–4454.
[38] Bahmani Jalali, H.; Sadeghi, S.; Baylam, I.; Han, M.; Ow-Yang, C. W.; Sennaroglu, A.; Nizamoglu, S. Exciton recycling via InP quantum dot funnels for luminescent solar concentrators. *Nano Res.* **2021**, *14*, 1488–1494.
[39] Song, W. S.; Lee, H. S.; Lee, J. C.; Jang, D. S.; Choi, Y.; Choi, M.; Yang, H. E. S. Amine-derived synthetic approach to color-tunable InP/ZnS quantum dots with high fluorescent qualities. *J. Nanopart. Res.* **2013**, *15*, 1750.
[40] Tessier, M. D.; De Nolf, K.; Dupont, D.; Sinnaeve, D.; De Roo, J.; Hens, Z. Aminophosphines: A double role in the synthesis of colloidal indium phosphide quantum dots. *J. Am. Chem. Soc* **2016**, *138*, 5923–5929.
[41] Jalali, H. B.; Sadeghi, S.; Dogru Yuksel, I. B.; Onal, A.; Nizamoglu, S. Past, present and future of indium phosphide quantum dots. *Nano Res.* **2022**, *15*, 4468–4489.
[42] Mundy, M. E.; Eagle, F. W.; Hughes, K. E.; Gamelin, D. R.; Cossairt, B. M. Synthesis and spectroscopy of emissive, surface-modified, copper-doped indium phosphide nanocrystals. *ACS Mater. Lett.* **2020**, *2*, 576–581.
[43] Huang, F.; Bi, C. H.; Guo, R. Q.; Zheng, C.; Ning, J. J.; Tian, J. J. Synthesis of colloidal blue-emitting InP/ZnS core/shell quantum dots with the assistance of copper cations. *J. Phys. Chem. Lett.* **2019**, *10*, 6720–6726.
[44] Eren, G. O.; Sadeghi, S.; Bahmani Jalali, H.; Ritter, M.; Han, M.; Baylam, I.; Melikov, R.; Onal, A.; Oz, F.; Sahin, M. et al. Cadmium-free and efficient type-II InP/ZnO/ZnS quantum dots and their application for LEDs. *ACS Appl. Mater. Interfaces* **2021**, *13*, 32022–32030.
[45] Grant, T. D. *Ab initio* electron density determination directly from solution scattering data. *Nat. Methods* **2018**, *15*, 191–193.
[46] Viswanatha, R.; Brovelli, S.; Pandey, A.; Crooker, S. A.; Klimov, V. I. Copper-doped inverted core/shell nanocrystals with "permanent" optically active holes. *Nano Lett.* **2011**, *11*, 4753–4758.
[47] Luo, B.; Liu, J. B.; Guo, H.; Liu, X.; Song, R.; Shen, K.; Wang, Z. M.; Jing, D. W.; Selopal, G. S.; Rosei, F. High efficiency photoelectrochemical hydrogen generation using eco-friendly Cu doped Zn-In-Se colloidal quantum dots. *Nano Energy* **2021**, *88*, 106220.
[48] Zhao, H. Y.; Li, X.; Cai, M. K.; Liu, C.; You, Y. M.; Wang, R.; Channa, A. I.; Lin, F.; Huo, D.; Xu, G. F. et al. Role of copper doping in heavy metal-free InP/ZnSe core/shell quantum dots for highly efficient and stable photoelectrochemical cell. *Adv. Energy Mater.* **2021**, *11*, 2101230.
[49] Kim, H. J.; Jo, J. H.; Yoon, S. Y.; Jo, D. Y.; Kim, H. S.; Park, B.; Yang, H. E. S. Emission enhancement of Cu-doped InP quantum dots through double shelling scheme. *Materials* **2019**, *12*, 2267.
[50] Hu, H. L.; Hao, H.; Ren, X.; Chen, Z. Y.; Liu, M.; Liu, Y.; Jiang, F. L. Bright InP quantum dots by mid-synthetic modification with zinc halides. *Inorg. Chem.* **2023**, *62*, 2877–2886.
[51] Liu, P.; Lou, Y. J.; Ding, S. H.; Zhang, W. D.; Wu, Z. H.; Yang, H. C.; Xu, B.; Wang, K.; Sun, X. W. Green InP/ZnSeS/ZnS core multi-shelled quantum dots synthesized with aminophosphine for effective display applications. *Adv. Funct. Mater.* **2021**, *31*, 2008453.
[52] Zhu, D. X.; Llusar, J.; Asaithambi, A.; Liu, Z. M.; Bes, R.; Prieur, D.; Karakkal, H. H.; Prato, M.; Brovelli, S.; Saleh, G. et al. Unveiling the role of $ZnCl_2$ in enhancing the photoluminescence efficiency of amino-as-based InAs@ZnSe quantum dots. *ACS Nano* **2025**, *19*, 34807–34818.
[53] Bradshaw, L. R.; Knowles, K. E.; McDowall, S.; Gamelin, D. R. Nanocrystals for luminescent solar concentrators. *Nano Lett.* **2015**, *15*, 1315–1323.
[54] Liu, X.; Luo, B.; Liu, J. B.; Jing, D. W.; Benetti, D.; Rosei, F. Eco-friendly quantum dots for liquid luminescent solar concentrators. *J. Mater. Chem. A* **2020**, *8*, 1787–1798.
[55] Liu, G. J.; Mazzaro, R.; Sun, C. C.; Zhang, Y. M.; Wang, Y. Q.; Zhao, H. G.; Han, G. T.; Vomiero, A. Role of refractive index in highly efficient laminated luminescent solar concentrators. *Nano Energy* **2020**, *70*, 104470.
[56] Li, H. B.; Wu, K. F.; Lim, J.; Song, H. J.; Klimov, V. I. Doctor-blade deposition of quantum dots onto standard window glass for low-loss large-area luminescent solar concentrators. *Nat. Energy* **2016**, *1*, 16157.
[57] Wu, K. F.; Li, H. B.; Klimov, V. I. Tandem luminescent solar concentrators based on engineered quantum dots. *Nat. Photonics* **2018**, *12*, 105–110.
[58] Meinardi, F.; Colombo, A.; Velizhanin, K. A.; Simonutti, R.; Lorenzon, M.; Beverina, L.; Viswanatha, R.; Klimov, V. I.; Brovelli, S. Large-area luminescent solar concentrators based on "Stokes-shift-engineered" nanocrystals in a mass-polymerized PMMA matrix. *Nat. Photonics* **2014**, *8*, 392–399.
[59] Meinardi, F.; Bruni, F.; Brovelli, S. Luminescent solar concentrators for building-integrated photovoltaics. *Nat. Rev. Mater.* **2017**, *2*, 17072.
[60] Yang, C. C.; Atwater, H. A.; Baldo, M. A.; Baran, D.; Barile, C. J.; Barr, M. C.; Bates, M.; Bawendi, M. G.; Bergren, M. R.; Borhan, B. et al. Consensus statement: Standardized reporting of power-producing luminescent solar concentrator performance. *Joule* **2022**, *6*, 8–15.
[61] Sadeghi, S.; Melikov, R.; Bahmani Jalali, H.; Karatum, O.; Srivastava, S. B.; Conkar, D.; Firat-Karalar, E. N.; Nizamoglu, S. Ecofriendly and efficient luminescent solar concentrators based on fluorescent proteins. *ACS Appl. Mater. Interfaces* **2019**, *11*, 8710–8716.

This is an open access article under the terms of the Creative Commons Attribution 4.0 International License (CC BY 4.0, https://creativecommons.org/licenses/by/4.0/).

© The Author(s) 2026. Published by Tsinghua University Press.